The Astrophysical Journal, 937:122 (12pp), 2022 October 1 https://doi.org/10.3847/1538-4357/ac8f27

The Expansion of the X-Ray Nebula Around η Car

Michael F. Corcoran[1,2], K. Hamaguchi[1,3], Nathan Smith[4], I. R. Stevens[5], A. F. J. Moffat[6], Noel D. Richardson[7], Gerd Weigelt[8], David Espinoza-Galeas[2,9], Augusto Damineli[10], Theodore R. Gull[11,12], and C. M. P. Russell[2]
[1] CRESST and X-Ray Astrophysics Laboratory, NASA/Goddard Space Flight Center, Greenbelt, MD 20771, USA; michael.f.corcoran@nasa.gov
[2] Institute for Astrophysics and Computational Sciences, The Catholic University of America, 620 Michigan Avenue, N.E. Washington, DC 20064, USA
[3] Department of Physics, University of Maryland, Baltimore County, 1000 Hilltop Circle, Baltimore, MD 21250, USA
[4] Steward Observatory, University of Arizona, 933 North Cherry Avenue, Tucson, AZ 85721, USA
[5] School of Physics and Astronomy, University of Birmingham, Edgbaston, Birmingham, B15 2TT, UK
[6] Département de physique and Centre de Recherche en Astrophysique du Québec (CRAQ), Université de Montréal, C.P. 6128, Succ. Centre-Ville, Montréal, Québec, H3C 3J7, Canada
[7] Embry-Riddle Aeronautical University, Physics and Astronomy Department, Prescott College of Arts & Sciences, 3700 Willow Creek Road, Prescott, AZ 86301, USA
[8] Max-Planck-Institut für Radioastronomie, Auf dem Hügel 69, D-53121 Bonn, Germany
[9] Departamento de Astronomía y Astrofísica, Facultad de Ciencias Espaciales, Universidad Nacional Autónoma de Honduras, Bulevar Suyapa, Tegucigalpa, M.D.C, Honduras
[10] Universidade de São Paulo, Instituto de Astronomia, Geofísica e Ciências Atmosféricas, Rua do Matão 1226, Cidade Universitária São Paulo-SP, 05508-090, Brazil
[11] Exoplanets & Stellar Astrophysics Laboratory, NASA/Goddard Space Flight Center, Greenbelt, MD 20771, USA
[12] Space Telescope Science Institute, 3700 San Martin Drive, Baltimore, MD 21218, USA
Received 2022 July 5; revised 2022 August 11; accepted 2022 September 1; published 2022 October 5

Abstract

The massive colliding wind binary system η Car is embedded in an X-ray emitting region having a characteristic temperature of a few million degrees, associated with ejecta produced during the 1840s, and in earlier outbursts. We use CHANDRA X-ray imaging observations obtained over the past two decades to directly measure the expansion of the X-ray nebula for the first time. A combined CHANDRA/ACIS image shows a faint, nearly uniform elliptic structure. This faint elliptical "shell" has a similar orientation and shape as the Homunculus nebula but is about 3 times larger. We measure proper motions of brighter regions associated with the X-ray emitting ring. We compare spectra of the soft X-ray emitting plasma in CHANDRA/ACIS and XMM-Newton PN observations and show that the PN observations indicate a decline in X-ray flux which is comparable to that derived from NICER observations. We associate the diffuse elliptical emission surrounding the bright X-ray "ring" with the blast wave produced during the Great Eruption. We suggest that the interaction of this blast wave with pre-existing clumps of ejecta produces the bright, broken X-ray emitting ring. We extrapolate the trend in X-ray energy back to the time of the Great Eruption using a simple model and show that the X-ray energy was comparable to the kinetic energy of the Homunculus, suggesting equipartition of energy between fast, low-density ejecta and slower, dense ejecta.

Unified Astronomy Thesaurus concepts: Proper motions (1295); High energy astrophysics (739); Circumstellar shells (242)

1. Introduction

The "Great Eruption," a giant outburst from the massive luminous binary system η Car in the middle of the 19th century (Herschel 1838; Smith & Frew 2011; Rest et al. 2012; Smith et al. 2018a) is one of the most impressive Galactic events in the modern history of astronomy. Starting in 1838, the system brightened by about 4 mag in the visible band (becoming the second-brightest star in the sky, despite its distance of 2.3 kpc) before fading to obscurity. This event was accompanied by a large ejection of mass which created the bipolar, dusty nebula today known as the Homunculus (Gaviola 1950). The Homunculus contains between 10 and $\gtrsim$45 $M_\odot$ of material (Smith et al. 2003; Morris et al. 2017). The expansion velocity of the Homunculus is about 600 km s^{-1}, so the kinetic energy of this outburst was $\gtrsim$4–16 $\times$ 10^{49} erg. This corresponds to a kinetic luminosity of $L \gtrsim 3$–13×10^7 $L_\odot$ over the 10 yr of the outburst, more than an order of magnitude larger than the current bolometric luminosity of the system. For comparison, the mass and radius of the star which is currently more luminous, η Car-A, is $\sim$90 $M_\odot$ and $\sim$60 $R_\odot$, respectively (Hillier et al. 2001), so the energy of the outburst amounts to $\gtrsim$10% of its gravitational binding energy.

Clues to the energetics and nature of this extraordinary event lie far beyond the Homunculus, in a region of optically bright clumps (sometimes called knots or condensations) of gas and dust collectively known as the "Outer Ejecta," "Outer Shell," or the "Outer Debris Field" (ODF; Thackeray 1949; Walborn 1976). Studies of the proper motions of the knots (Walborn et al. 1978; Walborn & Blanco 1988; Ebbets et al. 1993; Smith & Gehrz 1998; Morse et al. 2001) suggested that some of these ejecta were produced during the 19th century outburst, with evidence of at least 2–3 ejection episodes starting in the 13th century and spaced about two centuries apart (Kiminki et al. 2016). While the bulk of this material has velocities of a few hundred km s^{-1} (Kiminki et al. 2016), there is also evidence of much faster material associated with shock excitation. Smith & Morse (2004) suggested that fast-moving material from the Great Eruption fills the cavity between the Homunculus and older material in the ODF, producing a ring-

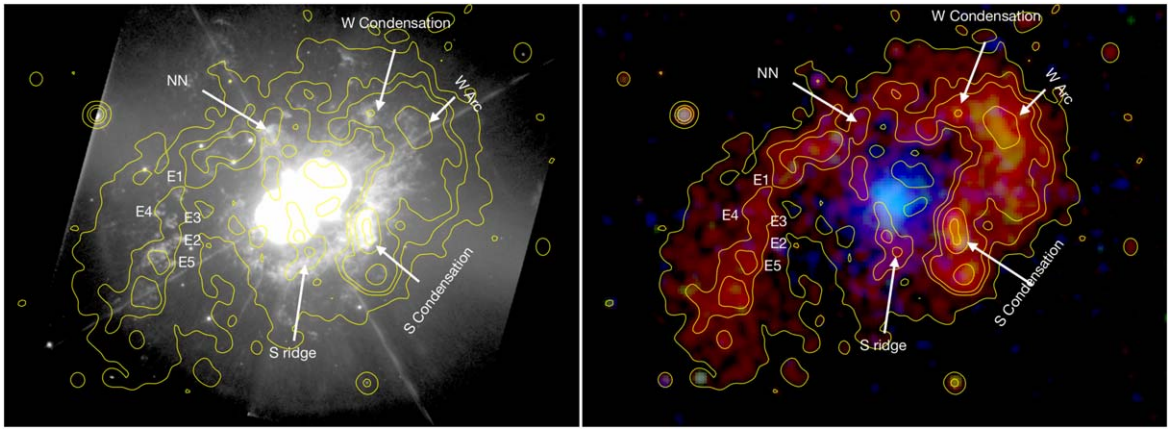

Figure 1. Left: a WFPC2 image using the F658N filter from 1999 June 12. The color scale has been chosen to emphasize the nebulosities in the ODF so that the Homunculus and the η Car binary system are saturated. Right: a "true-color" X-ray image from the CHANDRA/ACIS-I merged observation from 1999 September 26. The red channel is the soft band (0.5–1.2 keV), the green channel is the medium band (1.2–2.0 keV), and the blue channel is the hard band (2.0–7.0 keV). The X-ray contours from the red image are overlaid on the X-ray "true-color" image and on the WFPC2 image. The X-ray contour levels are 0.02, 0.08, 0.14, 0.40, and 1.0×10^{-6} photons s^{-1} cm^{-2}. Some identified optical features are labeled in both images.

like shock seen in soft X-ray images (Seward et al. 2001). Smith (2008) discovered extremely fast-moving ($V \gtrsim 1000$ km s^{-1}) ejecta from deep, long-slit optical spectra of the region around the Homunculus, proposed this as evidence of a strong blast wave from the Great Eruption, and noted that even a small amount of mass in these very fast ejecta would carry kinetic energy comparable to that of the more massive but slower Homunculus. In addition, spectroscopy of light echoes of the Great Eruption showed extremely fast outflow speeds ($V \sim 10{,}000$ km s^{-1}; Smith et al. 2018b), direct confirmation that the 19th century eruption was the source of the fast ejecta. However, because these observations only sampled a few discrete directions around the Homunculus, it was difficult to determine the overall energetics of the fast-moving material.

The energetics of the ejecta, and the timing of the ejection episodes, are keys to understanding the outburst mechanism. Smith et al. (2018a) presented evidence that the Great Eruption was a "two-stage" outburst, and proposed that the outburst was the final merger of two massive stars in a triple system, leaving behind the eccentric binary seen today. Hirai et al. (2021) presented a dynamical model of η Car as a massive triple system, and showed how the knots in the ODF could be evidence of sporadic ejections close to the orbital plane taking place over centuries, driven by orbital instabilities produced by interactions between the stars. However, other possibilities like massive accretion onto the companion (Soker 2004), pair-production instabilities (Woosley 2017) in the core of the more massive star, or enhanced nuclear burning during periastron passages, cannot yet be conclusively ruled out.

The visible knots in the ODF are embedded in an extended region of soft X-ray emission (Figure 1) first imaged by the EINSTEIN X-ray Observatory (Seward et al. 1979; Seward & Chlebowski 1982; Chlebowski et al. 1984), and subsequently by other X-ray observatories, notably ROSAT (Corcoran et al. 1995a, 1995b; Weis et al. 2001), CHANDRA (Seward et al. 2001) and XMM-Newton (Leutenegger et al. 2003). We call this X-ray emitting region the "X-ray Outer Debris Field" (XODF). Seward et al. (2001) argued that the apparent ring-like morphology of the extended X-ray emission indicates that the shocked gas has an actual ring-like geometry, rather than being a limb-brightened ellipsoidal shell. Analysis of spatially resolved X-ray spectra from a 91 ks CHANDRA/ACIS-S +HETG observation of the η Car field from 2000 November 19 by Weis et al. (2004) found shock temperatures in the XODF of 0.6–0.8 keV with little absorption, suggesting preshock velocities of 670–760 km s^{-1}, consistent with the proper-motion velocities of the clumps in the ODF. Mehner et al. (2016) combined Multi Unit Spectroscopic Explorer (MUSE) spectra at the Very Large Telescope with proper motions from the Hubble Space Telescope (Kiminki et al. 2016) and showed that the 3D structure of the outer ejecta can be described as a coherent "bent cylinder" with roughly the same symmetry axis as the Homunculus. They also showed that this structure is embedded in an X-ray "bubble" produced as the shell collides with the local interstellar medium at velocities of up to 3000 km s^{-1} (which, incidentally, is near the deduced terminal velocity of the wind from the companion star, η Car-B, Pittard & Corcoran 2002).

X-ray spectra of the brightest part of the X-ray emitting outer material near the "S-condensation" show a large N/O number ratio (>9, Leutenegger et al. 2003), and a similar nitrogen enhancement was also derived from analysis of UV spectra of the "S-condensation" (Davidson et al. 1982, 1986) and analysis of optical spectra (Smith & Morse 2004). The enhancement of nitrogen in the outer ejecta is usually understood to mean that the material was ejected by η Car-A during its core CNO burning stage, though Lamers et al. (1998) argued that the apparent chemical difference between the outer ejecta and the central binary meant that the star that produced the ejecta was actually the now-fainter companion, η Car-B, and not the Luminous Blue Variable primary star, η Car-A, we see today. The overabundance of nitrogen in at least parts of the XODF implies that the shocked material in the XODF is enriched young stellar ejecta (and not shocked interstellar gas).

The morphology and expansion of the hot, X-ray emitting, shocked ejecta in the XODF is an important complement to the optical proper-motion studies of the ejecta around η Car (Walborn et al. 1978; Walborn & Blanco 1988; Ebbets et al. 1993; Currie et al. 1996; Smith & Gehrz 1998; Morse et al. 2001; Kiminki et al. 2016; Smith 2017), providing unique information about the dynamical interactions between the fast-moving ejecta and the circumstellar medium. Combined with spatially resolved X-ray temperatures that measure the preshock speed of the ejecta (Weis et al. 2004), the X-ray

Table 1
CHANDRA/ACIS Imaging Observations of η Carinae

Seq Num	Obs ID	PI Name	Start Date	End Date	Duration (ks)	Exposure (ks)
290019	50	Calibration	1999-09-06 19:48:12	1999-09-06 23:46:37	14.3	11.9
280199	1249	Calibration	1999-09-06 23:45:34	1999-09-07 02:46:38	10.9	9.6
200237	4455	Corcoran	2003-08-28 17:37:04	2003-08-28 23:44:38	22.1	18.8
200549	9933	Hamaguchi	2009-01-10 19:08:07	2009-01-10 23:51:48	17.0	13.8
200550	9934	Hamaguchi	2009-01-16 01:25:51	2009-01-16 06:18:08	17.5	14.2
200551	9935	Hamaguchi	2009-01-22 06:40:54	2009-01-22 11:35:42	17.7	13.8
200552	9936	Hamaguchi	2009-01-29 06:30:55	2009-01-29 11:11:15	16.8	13.6
200553	9937	Hamaguchi	2009-02-03 14:15:37	2009-02-03 18:38:29	15.8	12.5
200944	16509	Hamaguchi	2014-08-04 08:30:23	2014-08-04 18:47:09	37.0	31.8
200944	15731	Hamaguchi	2014-08-06 22:24:43	2014-08-07 07:57:22	34.4	29.1
200945	15732	Hamaguchi	2014-08-18 21:08:05	2014-08-19 01:32:30	15.9	13.2
200945	16510	Hamaguchi	2014-08-22 19:36:18	2014-08-23 00:17:56	16.9	13.7
200946	15733	Hamaguchi	2014-09-08 06:37:35	2014-09-08 15:21:28	31.4	27.3
200946	16511	Hamaguchi	2014-09-15 16:09:30	2014-09-16 01:21:52	33.1	27.3
201281	22312	Corcoran	2020-02-22 20:02:13	2020-02-23 05:04:33	32.5	27.3
201282	22313	Corcoran	2020-03-06 20:00:08	2020-03-06 23:14:50	11.7	9.1

emission helps to constrain the energetics of the expansion of the shocked gas in 3D. The expansion of the XODF has not previously been directly measured, mostly due to the coarse spatial resolution of most imaging X-ray observatories which have observed the η Car system. Measurement of this expansion has previously been challenging even at the 0.″5 resolution of CHANDRA.

As part of an X-ray campaign to monitor the X-ray spectral variability of the colliding wind emission from η Car near periastron passage of the binary, CHANDRA has observed η Car roughly every 5 yr beginning soon after launch in 1999. These CHANDRA observations now provide a baseline stretching over more than two decades (during which time material from the Great Eruption should have expanded by $\sim$12%). At the distance of η Car, $d \approx 2300$ pc, this means that motions with proper velocities of $\gtrsim 500\,\mathrm{km\,s^{-1}}$ are currently detectable by comparing CHANDRA images over the life of the mission.

In this paper, we examine the expansion of the XODF based on more than 20 yr of CHANDRA imaging observations. We show the existence of a faint elliptical X-ray shell of fairly uniform surface brightness surrounding the more noticeable, X-ray bright ring discussed in earlier studies. We report the first measures of X-ray motion of discrete features in the XODF associated with the "S-ridge," the "W-arc," and the eastern condensations. We compare the observed X-ray proper motions with those found from optical studies, and examine, in a limited way, the spatial distribution of the proper velocities.

This paper is organized as follows. In Section 2, we list the relevant CHANDRA observations and discuss the reduction and alignment of the X-ray images. In Section 3, we discuss the shape of the diffuse X-ray emission around η Car from combined ACIS images. We present exposure-corrected color images of the XODF from 5 epochs in Section 4. In Section 5, we spatially compare the aligned images to look for changes in bright emission regions in the XODF. We discuss our results on the expansion of the XODF and the energetics of the Great Eruption and compare our results to earlier work in Section 6. We summarize our conclusions in Section 7.

2. Archival CHANDRA Imaging Observations of η Car

Table 1 lists the CHANDRA/ACIS imaging (nongrating) observations of η Car in timed-event mode. There are also currently 44 ACIS observations in the CHANDRA archive within 1′ of η Car taken with the High Energy Transmission Grating in place. These observations have potentially useful spatial information at zeroth order (and indeed one such observation from 2000 was used by Weis et al. 2004, in their spectral-spatial analysis of the XODF), but because the HETG reduces sensitivity at low energies in addition to the buildup of obscuring contamination on the ACIS optical blocking filter,[13] these observations for the most part are of limited use for measuring small changes in the soft, faint extended emission in the XODF, so we do not discuss them further. Neither do we consider observations where η Car was observed more than 3′ off-axis, since spatial resolution decreases with increasing off-axis angle. Therefore we excluded from our analysis CHANDRA OBSID 6402 (an ACIS-I imaging observation of Trumpler 16 in which η Car was placed about 3.′5 from the aimpoint).

The most recent ACIS nongrating, timed-event mode observations were obtained in February and March of 2020. The earliest nongrating observations were obtained in 1999 September, only 45 days after CHANDRA's launch. Comparison of these first observations with the 2020 images allows us to examine spatial variations over a 20 yr time span. Note that the 1999 data were obtained with ACIS-I in a "warm" (T = -100°C) state which affects the event energy correction for photon events in this observation, but which should produce no significant spatial issues. Table 1 lists the Observation IDs (OBS IDs) of the CHANDRA data sets considered here. All the images were obtained using the back-illuminated CHANDRA/ACIS-S3 detector, except for the 1999 observations, OBS ID 50 and 1249, which were obtained using the front-illuminated ACIS-I3 detector.

After retrieving the observations listed in Table 1 from the CHANDRA archive, we reprocessed them using the `chandra_repro` processing script using version 4.9.0 of the CHANDRA calibration database (CALDB) and version 4.12 of

[13] See https://cxc.cfa.harvard.edu/ciao/why/acisqecontamN0014.html.

Table 2
Merged Observations

Year	Start Date	End Date	Span (days)	Total Exposure (ks)	OBSIDs
1999	1999-09-06 19:48:12	1999-09-06T23:46:37	0.17	21.51	50, 1249
2003	2003-08-28 17:37:04	2003-08-28T23:44:38	0.26	18.8	4455
2009	2009-01-10 19:08:07	2009-02-03T18:38:29	23.98	67.9	9933, 9934, 9935, 9936, 9937
2014	2014-08-04 08:30:23	2014-09-16T01:21:52	42.70	142.3	16509, 15731, 15732, 16510, 15733, 16511
2020	2020-02-22 20:02:13	2020-03-06T23:14:50	13.13	36.4	22312, 22313

the CHANDRA Interactive Analysis of Observations (CIAO; Fruscione et al. 2006) software provided by the CHANDRA X-ray Center. Before determining proper motions, we corrected the individual reprocessed observations for misalignments in the absolute astrometry (which can be as large as 0.″4, corresponding to errors of $\delta V \sim 200\,\mathrm{km\,s^{-1}}$ in proper velocity over a 20 yr span). We first aligned all the individual observations according to the "reproject aspect"[14] thread published by the Chandra X-ray Center. For each observation in Table 1, we used the "align_wcs" CIAO script to adjust the absolute astrometry using the same list of cataloged X-ray sources within 2′ of η Car from the Chandra Source Catalog, version 2.0 (Evans et al. 2020). We excluded obvious sources associated with the nebulosity in the XODF and η Car itself since the ACIS images of the star suffer from photon pileup. This resulted in a table of 36 point-like X-ray sources which were used for aspect correction and spatial alignment. Visual comparison of the aligned images showed good agreement with the cataloged optical locations of known X-ray emitting point sources. We merged the individual aligned images by year in order to improve signal-to-noise and to minimize spatial blurring due to proper-motion. Table 2 lists the individual observations that were used to construct merged images for observations in 1999, 2003, 2009, 2014, and 2020.

Figure 1 compares the merged, aligned X-ray image from the 1999 CHANDRA observations to a contemporaneous optical image from HST. The left panel of Figure 1 shows HST/WFPC2 optical image from 1999 with some optical features in the ODF marked, while the contemporaneous X-ray "true-color" image is shown on the left, with the optical features marked. X-ray contours from the 1999 soft-band image are overlaid on both the "true-color" X-ray image and the HST/WFPC2 image. The comparison shows that the S-condensation and S-ridge complex, the W-arc and W-condensation, and the E-condensations, correspond to regions of enhanced X-ray emission.

3. Evidence of an X-Ray Blast Wave from the Merged CHANDRA Image

To better examine the faint structure and the boundary of the XODF, we merged all the coaligned ACIS observations listed in Table 2. Figure 2 shows a false-color image in the $0.1 < E < 1.0$ keV band from the merged X-ray observations, along with X-ray contours. The image on the right is the WFPC2 F658N filter from 1999 June 12 shown in Figure 1. This false-color merged X-ray image again shows a good correlation between bright X-ray regions and the optical knots. The bright X-ray emitting "ring" (shown in pink/red in the false-color image, from the S-ridge counterclockwise through the E-condensations) seems more continuous than the clumped optical nebulosity, with an apparent decrease in brightness between the S-ridge and the E-condensations.

Importantly, the merged, smoothed soft-band X-ray image also reveals the existence of a faint elliptical shell at a level of 5–10 ACIS counts surrounding η Car and the ODF and apparently extending well beyond the bright X-ray emitting ring. This shell has a more uniform surface brightness compared to the bright X-ray emitting ring, and fills the apparent gap in the ring between the S-ridge and the E-condensations. The apparent orientation of the ellipse and its ellipticity, $b/a = 0.67$ (where a and b are the projected semimajor and semiminor axes, respectively) seem consistent with the shape and orientation of the Homunculus, suggesting a common origin for both structures. The X-ray structure is about three times larger than the Homunculus, suggesting proportionally higher speeds if both originated at the same time. We suggest that this faint X-ray emitting shell represents a fast blast wave associated with the eruption of 1843, as inferred by Smith (2008) from optical spectra along selected directions to the northwest and east of the star. The X-ray image gives a more complete view of the blast wave projected on the sky and shows that the shocked gas completely surrounds η Car and the Homunculus. The shell extends to a projected distance of ≈22″ from η Car in the northwest and ≈36″ from η Car in the southeast. If this shell was produced by η Car during the Great Eruption, this separation corresponds to a proper velocity slightly in excess of $2000\,\mathrm{km\,s^{-1}}$. The extended X-ray emission can be approximated in projection by an ellipse with a semimajor axis of $a = 43''$ and semiminor axis of $b = 28''$, so that the volume V of the ellipsoid is about $6.1 \times 10^{54}\ \mathrm{cm^{-3}}$ at a distance of 2300 pc, while the emission measure of the shell, EM is about $4 \times 10^{55}\ \mathrm{cm^{-3}}$ (Espinoza-Galeas et al. 2022). Thus the density $n_{\mathrm{H}} = \sqrt{\mathrm{EM}/V} \sim 1.6\,\mathrm{cm^{-3}}$, and the mass of the hot shocked material in the XODF is $0.012\,M_{\odot}$, assuming a pure H composition and that the material uniformly fills the volume.

The blast wave in Figure 2 is similar to the X-ray "bubble" noted by Mehner et al. (2016) which surrounds the outer shell they found in their analysis of MUSE spectro-images of the region around η Car and the Homunculus. This suggests that the X-ray emission is probably the forward shock produced by the ejection of this outer shell moving at velocities of $\sim$2500 km s^{-1} (Mehner et al. 2016).

4. Examining Changes in X-Ray Color

We created three-color RGB images of the merged data sets to examine potential changes in characteristic X-ray energy over the 20 yr span of the CHANDRA observations and to aid in the identification of discrete features. We used the aligned X-ray event files and the corrected aspect solutions to create

[14] See https://cxc.cfa.harvard.edu/ciao/threads/reproject_aspect/.

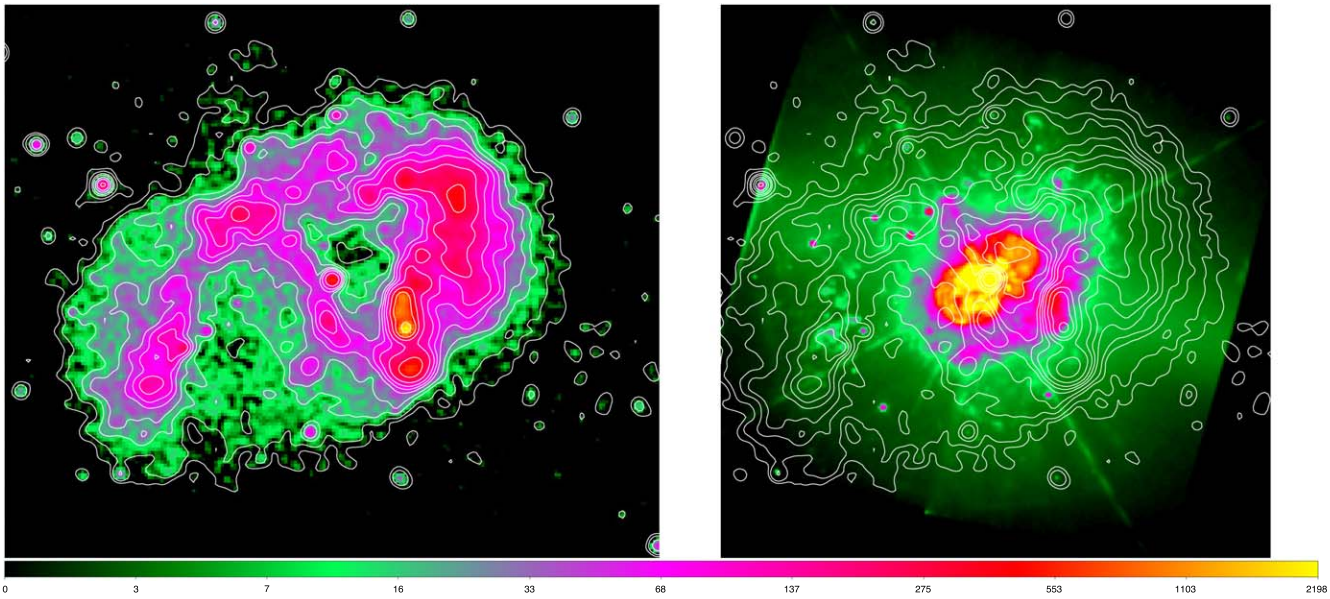

Figure 2. Left: a false-color soft-band ($0.1 < E < 1.0$ keV) CHANDRA/ACIS image obtained by merging all the observations listed in Table 2. The total exposure is 286.9 ks. The image has been smoothed by a Gaussian kernel with a radius of 2 pixels and a sigma of 1 pixel. The image is not exposure corrected. Contour levels are 0.6, 1.0, 2.0, 3.0, 5.0, 7.0, 10.0, 16.0, 30.0, 50.0, and 100 counts in the merged, smoothed image. Right: the WFPC2 F658N filter from 1999 June 12 compared to the merged X-ray contours.

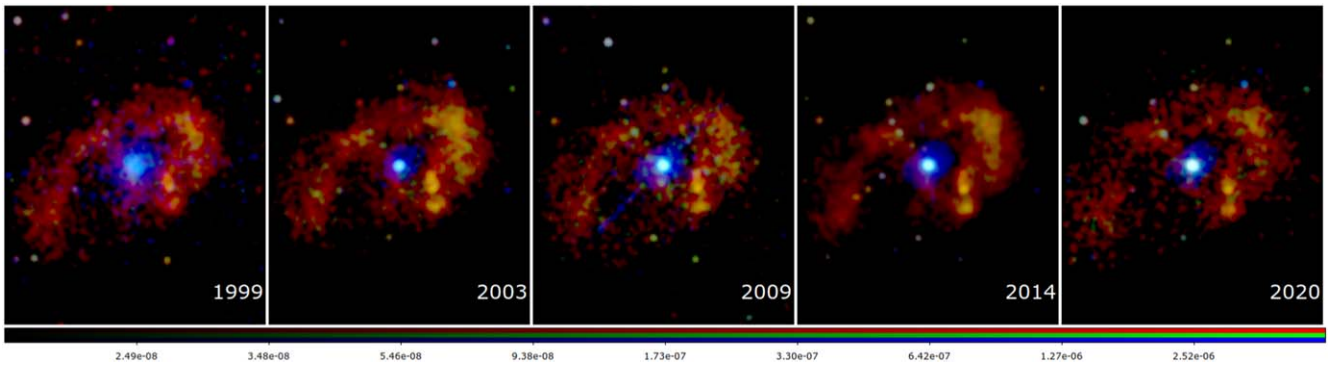

Figure 3. A comparison of "true-color" flux images of the Outer Debris Field around η Car, from 1999 through 2020. Red = 0.5–1.2 keV; green = 1.2–2.0 keV; blue = 2.0–7.0 keV. The blue band is dominated by the emission from the colliding wind source associated with the η Car binary system, and varies depending on the orbital phase, while the emission from the X-ray Outer Debris Field is most prominent in the red and green bands. The flux scale in photons s^{-1} cm^{-2} used to display the red, green, and blue bands is given along the bottom. A number of the X-ray emitting point sources in the field vary over the time span of these observations. The images used a different color scaling for the red, green, and blue channels, but used the same scaling for each color channel for all the images.

exposure-corrected images and exposure and point-spread function maps in the broad (0.5–7.0 keV), soft (0.5–1.2 keV), medium (1.2–2.0 keV), and hard (2.0–7.0 keV) energy bands using the CIAO `fluximage` tool. Exposure correction is important in order to account for the decline in ACIS soft-band sensitivity over time due to the buildup of contamination on the ACIS optical blocking filter. We used an encircled counts fraction = 0.9 to generate maps of the point-spread function. We then used the exposure-corrected soft, medium, and hard band images as red, green, and blue channels (respectively) in the RGB color images.

Figure 3 compares the color images from the five individual observations from 1999 to 2020. The hard, locally absorbed colliding wind emission from the η Car binary system saturates the center of the images, but the soft, mostly unabsorbed emission from the XODF is unsaturated. The discrete structures in the XODF show no obvious color change in the exposure-corrected images during this 20 yr time span.

5. X-Ray Expansion

5.1. Radial Profiles

To establish the bulk motion of the X-ray emitting shocked gas in the XODF, we calculated radial profiles[15] of the diffuse X-ray emission around η Car from the 1999 and 2020 merged soft-band observations. Assuming homologous expansion, we used 20 equally spaced elliptical annuli ($e = 0.61$) rotated by an angle $\theta = 39°$ east of north (which approximates the apparent orientation and ellipticity of the X-ray emitting ring around η Car), centered on the pixel position of η Car in each image (Figure 4). The annuli extended from $9\farcs8$ to $45''$ along the major axis away η Car. The radial surface brightness profiles were exposure corrected and background subtracted (at a level of about 0.03 counts $pixel^{-2}$ for the 2020 observation and 0.02 counts $pixel^{-2}$ for the 1999 observation), where the

[15] See the "Obtain and Fit a Radial Profile (https://cxc.harvard.edu/ciao/threads/radial_profile/)" `CIAO` science thread for details.

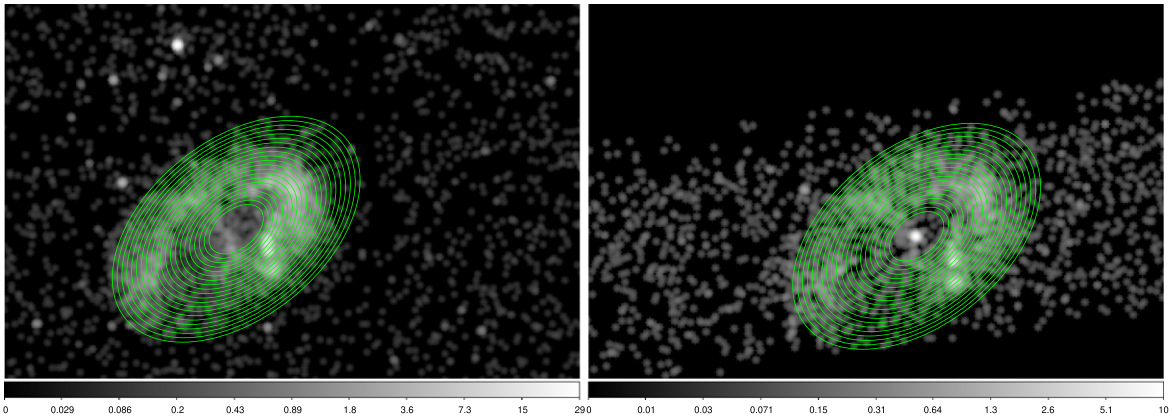

Figure 4. Elliptical annuli used to extract the radial profile of the XODF. Left: 1999 image. Right: 2020 image. The images have been smoothed by using a Gaussian kernel with radius = 3 pixels and $\sigma = 1.5$ pixels for display purposes. The radial profiles were extracted using unsmoothed, unbinned images.

background was derived in circular, source-free regions outside the XODF. The profiles were normalized to the first radial bin to account for residual differences and the decline in the brightness of the XODF in the 21 yr interval (Espinoza-Galeas 2021; Espinoza-Galeas et al. 2022). A comparison of the derived profiles (Figure 5) shows that the peak emission in the shell has shifted outward by about 3″ in the 2020 image compared to the 1999 image. A shift of 3″ in the 21 yr between the observations corresponds to a proper expansion rate of ≈1500 km s^{-1}. This is faster than the speed of the dense optical knots (300–400 km s^{-1}) so that the shell is not a standing shock but rather moving through the optical knots and expanding past them.

5.2. Image Comparison and the Motion of Individual Features

Figure 6 compares the merged, exposure-corrected soft-band false-color images from 1999 and 2020. The agreement between stellar X-ray point sources visible in both the 1999 and 2020 observations indicates that both images are aligned to <0.″1. Contours from the 1999 image are overlaid on both the 1999 and 2020 images. Clearly, some features in the 2020 image have moved past the corresponding contour from the 1999 image. Quantifying the expansion of X-ray features in the XODF is challenging, however, since even the bright features are diffuse and rather faint, making centroiding difficult; other features are compact and so may be confused with X-ray emitting stars or other point sources in the ODF. Apparent positional variability may also instead reflect actual source variability (either intrinsic to the feature, or due to changing soft-band sensitivity of the ACIS detector). However, Figure 3 shows little evidence of color variations over time, suggesting that any induced spatial variability due to changes in ACIS soft-band sensitivity is probably minimal in the exposure-corrected images.

To help quantify the X-ray motion of individual features, Figure 7 shows a difference image between the 2020 merged, exposure-corrected soft-band image and the 1999 merged, exposure-corrected soft-band image. The 2020 image was scaled by the ratio of the mean of the 1999 soft-band image to the mean of the 2020 soft-band image to adjust for residual differences in soft-band sensitivity and intrinsic brightness changes in the XODF between the two images. The difference image is shown using a linear grayscale color map. Regions near the S-ridge, the W-arc, and the E-condensations show significant evidence of expansion—regions near η Car in the

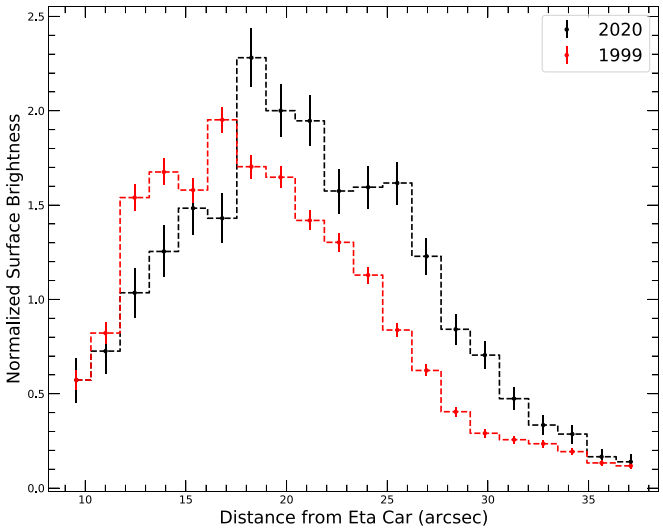

Figure 5. Surface brightness (photons cm^{-2} pixel^{-2} s^{-1}) in the 20 elliptical annuli shown in Figure 4 for the 1999 merged ACIS observation and the 2020 merged observation, plotted vs. offset from the optical location of η Car along the major axis. The surface brightnesses were background subtracted and normalized to the surface brightness of the first radial bin.

1999 image are brighter than those regions in the 2022 image (producing negative residuals), while regions further from η Car are brighter in the 2020 image compared to the 1999 image (producing positive residuals). We note that the soft emission from η Car itself has brightened between 2020 and 1999. This is likely due to a combination of increased photon pileup in the 1999 ACIS-I image, along with the decline of localized absorption along our line of sight to the star (Damineli et al. 2021).

The arrows show some expansion vectors for selected bright X-ray knots around the XODF. The expansion is assumed to be in the (projected) radial direction from η Car, and each vector begins near a negative extremum in the difference image and ends near a positive extremum along the radius vector in the outward direction. Table 3 shows the proper motions, distances, velocities, and position angles (north through east) for the selected features. In Figure 7, different colors are used to represent vectors of different vector lengths δl: yellow: $\delta l < 2''$; green: $2'' \lesssim \delta l < 3''$; cyan: $3'' \lesssim \delta l < 4''$. Detailed comparison of bright regions (such as the ones near the S-ridge) show apparent brightness differences as well; some

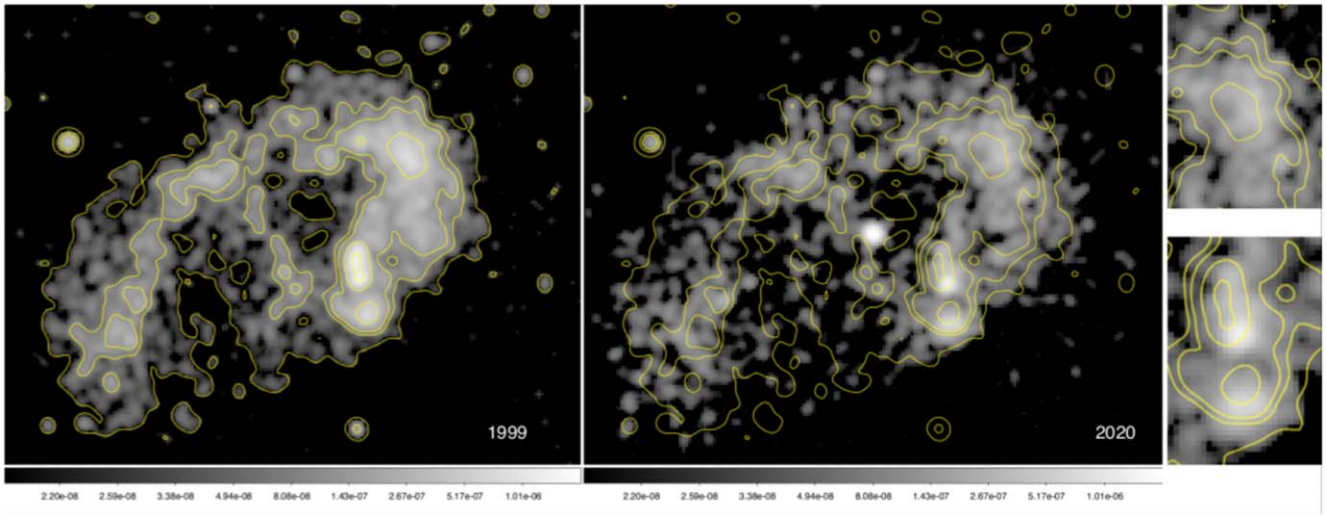

Figure 6. Left: merged, exposure-corrected soft-band ACIS-I false-color image from 1999 and image contours. The X-ray contour levels are 0.02, 0.08, 0.14, 0.40, and 1.0×10^{-6} photons s^{-1} cm^{-2} as used in Figure 1. Middle: merged, aligned 2020 soft-band ACIS-S false-color image with the contours from the 1999 ACIS-I observation overlain. Right: bright regions in the XODF near the S-condensations/S-ridge and W-arc which show clear expansion. In addition, the outermost emission associated with the XODF in 2020 is larger than the boundary of the outermost contour from the 1999 image. The agreement in the location of stellar X-ray point sources between the image and the contours show that the alignment between the images is $<0\farcs1$. Images are displayed using a logarithmic scale between $(0.02–2) \times 10^{-6}$ photons s^{-1} cm^{-2}.

regions in the 1999 image seem to grow brighter in the 2020 image, if the expansion is all in the (projected) radial direction. This change may be due to density inhomogeneities in the circumstellar medium which the blast wave encounters as it moves outwards. However, we again note that the earliest two ACIS imaging observations in Table 1 (Obs IDs 50 and 1249) were obtained at a focal plane temperature of −100°C (rather than the standard temperature of −119.7°C) and therefore these two do not have reliable spectral calibrations (Seward et al. 2001), so some care needs to be taken when evaluating positional differences in the XODF between these two observations and more recent ones.

5.3. Evidence of Additional Brightness Variations

In addition to displacements, some features in the XODF undergo apparent brightness variations. Figure 8 compares the broadband (0.2–10 keV) images from the merged 1999 and the merged 2020 observations. We adjusted the color scale individually in each image so as to display features with comparable contrast. Brightness contours from the 2020 observation are displayed on each image. The apparent outward motions from 1999 to 2020 of the S-ridge, S-condensation, W-arc, and the E-condensations features seen in the soft-band image (Figure 6) are also apparent in this broadband image. But some "stationary" features seem to have changed brightness at the same location. We have labeled some features in the 1999 image which seem to have changed brightness in the 2020 image. These "stationary" features may be X-ray variable point sources not associated with the XODF, or slow-moving features whose brightness changes as the blast wave moves by them.

6. Discussion

6.1. Comparison to Optical Proper Motions

Kiminki et al. (2016) measured nearly 800 optical knots in the ODF, and they show that they have a bimodal velocity distribution (see Figure 4 in that paper), with a large peak near 400 km s^{-1}, a smaller peak near 900 km s^{-1}, and a high-velocity tail extending out to more than 1400 km s^{-1}. Knots near the S-condensations and S-ridge show a mix of velocities peaked at about 400 km s^{-1}; knots near the E-condensations show a narrower distribution in velocity with a peak near 400 km s^{-1}. Broader distributions in velocity extending beyond 800 km s^{-1} up to more than 1000 km s^{-1}, were found near the upper part of the S-ridge and the region of the W-arc and W condensations. Even faster ejecta are seen in optical spectra (Smith 2008), but most of these cannot be seen in HST images because their motion is not in the plane of the sky, and they are Doppler shifted out of the narrowband filters used. Smith (2008) and Smith et al. (2018b) presented evidence for high-velocity ejecta at velocities of >1000 up to 10,000 km s^{-1}.

The X-ray emitting regions in the difference image show proper velocities in the range of 1000–2000 km s^{-1}. The feature we have labeled "Wa" in Figure 7, associated with the "W-arc" optical feature, has the largest measured proper velocity, $V \approx 2126$ km s^{-1}. Kiminki et al. (2016) also found some of their highest measured proper velocities ($\gtrsim$1000 km s^{-1}) for the optical knots near the W-arc. The features marked "EX1" and "Sc3" in Figure 7 also have proper velocities in excess of 2000 km s^{-1}.

6.2. The Bright X-Ray "Ring" and the Faint Elliptical Shell

The analysis of the bright X-ray ring in the outer debris field by Weis et al. (2004) showed that the temperature around the ring was fairly uniform, 0.6–0.8 keV, though with some evidence of spatial variation. This temperature range implies a rather narrow range in preshock velocities (670–760 km s^{-1}), consistent with the measured expansion velocity of the optical knots. They suggested that the bright, broken X-ray ring is the hot shocked gas produced when fast-moving clumps of ejecta plow into a stationary circumstellar medium (with perhaps some contribution from collisions between individual knots). This interpretation did not address the spatial distribution of the clumps or the relation to the bipolar Homunculus if both were produced by the large eruption in the 1840s.

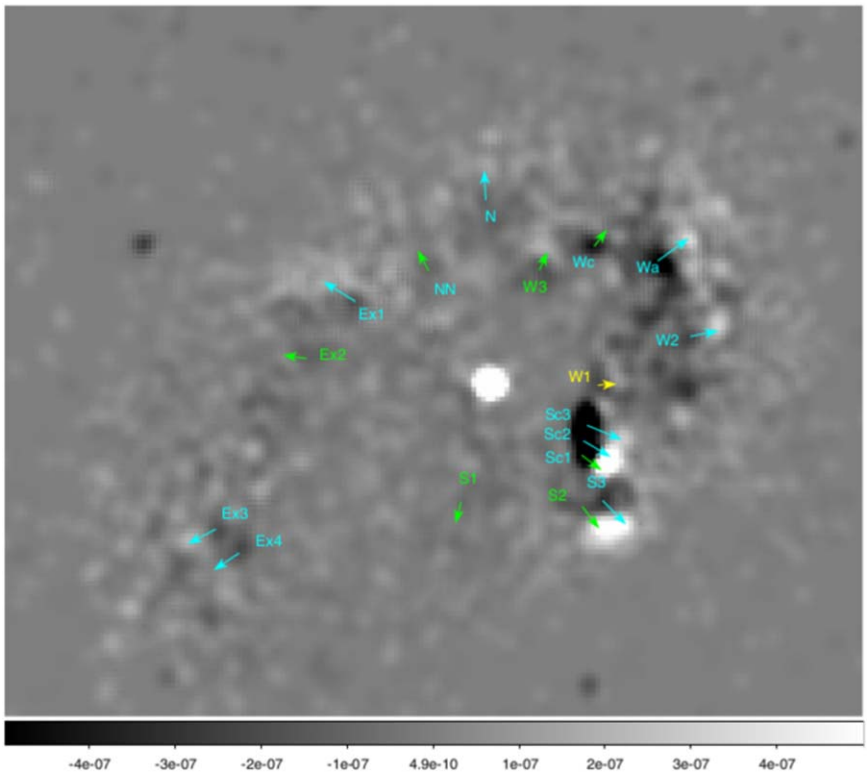

Figure 7. Difference image between the 2020 merged, exposure-corrected soft-band image and the 1999 merged, exposure-corrected soft-band image. The 2020 merged image has been multiplied by the ratio of the mean of the 1999 image to the mean of the 2020 image to approximately remove residual differences in soft-band sensitivity. The arrows mark prominent regions of expansion, assumed to be directed along projected radii from η Car. The color map is scaled in units of photons s^{-1} cm^{-2}.

Table 3
Motions of Marked Knots

ID	PM ($''$ yr^{-1})	PA (°)	Distance from η Car ($''$)	PV (km s^{-1})
W1	0.093	273.3	11.2	1012
W3	0.103	336.3	12.9	1119
Wc	0.108	322.8	17.9	1172
S1	0.112	166.5	12.4	1226
NN	0.117	27.8	13.3	1279
Ex2	0.122	81.7	19.0	1332
Sc1	0.127	232.9	12.0	1385
S3	0.142	217.5	15.8	1545
W2	0.147	281.9	21.3	1598
N	0.151	1.2	19.1	1652
Ex4	0.156	123.9	31.1	1705
Sc2	0.161	239.4	11.3	1758
Ex3	0.161	117.8	31.9	1758
S3	0.171	224.5	16.7	1865
Sc3	0.191	247.6	10.9	2078
Ex1	0.191	58.0	16.3	2078
Wa	0.195	306.3	21.6	2126

The faint elliptical region of soft X-ray emission revealed in Figure 2 offers a somewhat different interpretation of the origin of the X-ray bright ring in the XODF. We interpret the fairly uniform surface brightness of the faint elliptical X-ray emission (which even nearly fills the apparent gap in the X-ray "ring" between the S-ridge and the E-condensations) as the blast wave from the Great Eruption in the 19th century as discussed by Smith (2008) and Mehner et al. (2016). If this is correct, then the uniform morphology of this emission indicates that the blast wave was nearly symmetric and indeed completely surrounds η Car. The blast wave would have freely expanded into a region nearly evacuated by the winds from the η Car system at a velocity of $\sim$2000 km s^{-1}, as indicated by the extent of the faint emission. The apparent elliptical shape of the shell is either intrinsic to the eruptive event, or a result of the shape of the circumstellar cavity around η Car produced by nonspherical winds from the system. Given the similarity of this outer X-ray emission to the shape and orientation of the Homunculus, it likely indicates that the morphology was intrinsic to the eruption. Kiminki et al. (2016) showed that many of the knots in the ODF originated in events prior to the eruption of 1843, some dating back to the 13th and 16th centuries. The analysis of the X-ray surface brightness of the X-ray bright ring by Seward et al. (2001) suggested that the bright outer X-ray emission was indeed ring-like, rather than a limb-brightened shell. Thus the X-ray emission from the XODF can be interpreted as a near uniform, elliptical, high-velocity, low-density blast wave produced during the Great Eruption. The collision of this blast wave with a ring of dense, pre-existing clumps of ejecta distributed largely in a plane produces the bright X-ray emitting ring around the Homunculus. This seems consistent with the scenario proposed by Smith et al. (2018a) in which the large eruption in the middle of the 19th century was produced by the merger of an inner binary in a triple system, with close encounters between the stars in the inner binary in the centuries prior to the merger event producing "sprays" of ejecta preferentially located near the orbital plane of the inner binary, as also shown in the numerical three-body simulations of Hirai et al. (2021).

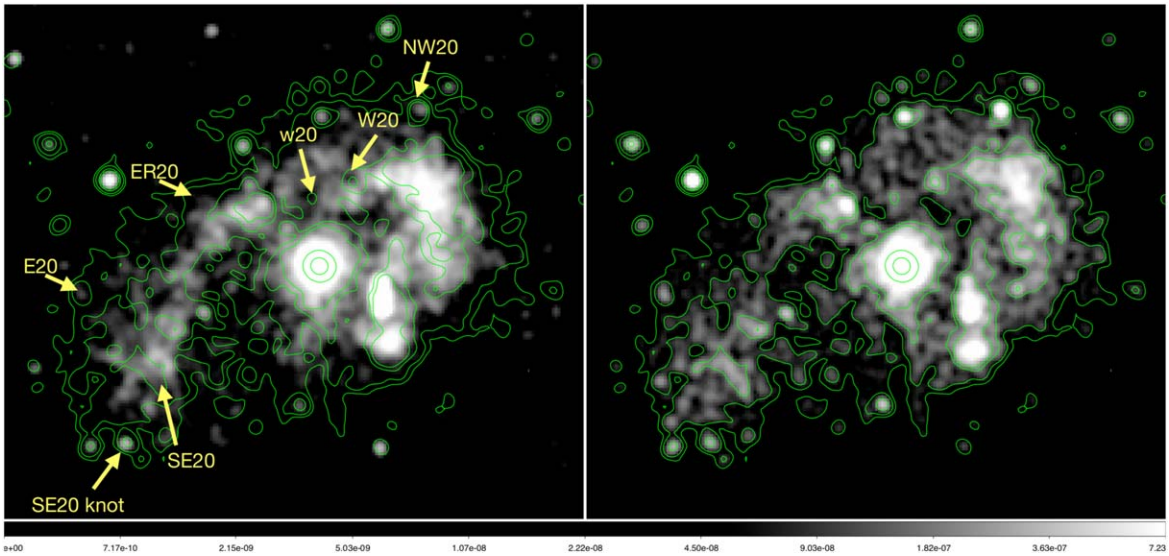

Figure 8. Comparison of exposure-corrected merged broadband CHANDRA/ACIS images from 1999 (left) and 2020 (right). Contours from the 2020 broadband image are overlain on both images. Features marked in the 1999 image show apparent changes over the time span of the two images.

The comparison of a rotated, elliptical annulus centered on η Car to the merged 2020 soft-band image implies that the outer emission has a projected semimajor axis of $43\farcs4$ and eccentricity $e = 0.53$. Assuming the shell has the same inclination to our line of sight as the Homunculus, $i = 41\fdg0$ (Davidson et al. 2001; Smith 2006; Mehner et al. 2016), then the outer radius of the faint X-ray shell is $\approx 3.5 \times 10^{18}$ cm. If the blast wave follows a Sedov–Taylor expansion, then the ambient density is given by $\rho \approx 2ET_o^2/r_s^5$ (Borkowski et al. 2001), where E is the energy of the blast, T_o the time since the explosion, and r_s the current radius of the blast wave. Taking $E \approx 4 \times 10^{49}$ erg, $To \approx 177$ yr, then in the direction of the major axis of the XODF ring the particle density $n \sim 3$ cm^{-3}, while in the perpendicular direction, $n \sim 300$ cm^{-3}, if the ellipticity of the shell is caused by a variation in ambient density.

From a spatially resolved analysis of the X-ray spectra around the XODF, Weis et al. (2004) derived an average temperature for the shocked gas of 7.0–8.8 MK, corresponding to relative preshock velocities of ~670–760 km s^{-1}. These velocities were found to be similar to measured velocities of the optical knots in the ODF, which suggested to Weis et al. (2004) that the X-ray emission in the XODF was from shocked gas produced by the collision of the optical knots with the ambient medium. In this picture, the relative velocity between the blast wave (~2000 km s^{-1}) and the fast-moving ejecta (~250–1400 km s^{-1}) would account for the relatively low X-ray temperatures measured by Weis et al. (2004) in the bright X-ray ring. The blast wave will also accelerate the optical knots in the Outer Debris Field. This means in principle that deriving average velocities of clumps from proper-motion studies which assume constant velocity would overestimate the true average clump velocity over its lifetime, and thus underestimate the clump age distribution. However, little acceleration of the optical knots has been seen in proper-motion studies (Kiminki et al. 2016).

6.3. Energetics of the Expanding Hot Gas

Recently, Espinoza-Galeas (2021) and Espinoza-Galeas et al. (2022) examined the time dependence of η Car's X-ray emission using NICER observations centered on η Car over the 2017–2020 interval. NICER is a non-imaging X-ray facility berthed on the International Space Station, which has a large effective area in the 0.5–10 keV band, with a field of view that is restricted to about 3 arcmin^2. Espinoza-Galeas et al. showed that the emission arising from the XODF in the $0.5 < E < 1.0$ keV band exhibited a nearly linear decline over the interval of the NICER observations they studied (in contrast to the 2–10 keV emission which varies with the orbital phase of the binary). They also showed that the observed decline was consistent with the X-ray emission measure decline expected from the free expansion of an isothermal region of shocked gas which should vary with time t as t^{-3}. Extrapolating back in time, they derived an X-ray luminosity, $L_x \gtrsim 3 \times 10^{41}$ erg s^{-1} a few weeks after the Great Eruption. The X-ray luminosity of this "instantaneous" blast wave is enormous and comparable to (and perhaps greater than) the (non-X-ray) bolometric luminosity of the system at longer wavelengths, $L_{\rm bol} \sim 0.8 \times 10^{41}$ erg s^{-1}, as calculated by Davidson & Humphreys (1997). Smith (2013) previously suggested that η Car would have had a large X-ray luminosity during the Great Eruption.

The expansion derived from the decline in the X-ray emission measure by Espinoza-Galeas et al. (2022) is consistent with the expansion velocities derived from the CHANDRA/ACIS images. From Table 3, the average proper velocity for the X-ray knots is $\langle \mathrm{PV} \rangle = 1570$ km s^{-1}, while the average projected separation of the knots from η Car is $\langle \mathrm{d} \rangle = 17''$. These averages are consistent overall with the expected separations and velocities for freely expanding shocked gas from an eruption occurring near 1843, $V \approx 1000$ km s^{-1}.

To further explore the decline in the X-ray flux from the XODF reported by Espinoza-Galeas et al. (2022), we examined the soft-band emission from three ACIS observations from 2009 (OBSID 9944) 2014 (OBSID 16509), and 2020 (OBSID 22312), along with four XMM-Newton PN observations covering the 2003–2015 interval (XMM-Newton sequences 0145740101, 2003 January 25; 0311990101, 2006 January 31; 0560580101, 2009 January 5; and 0762910401, 2015 July 16). We used the XMM-Newton PN event files from the archived

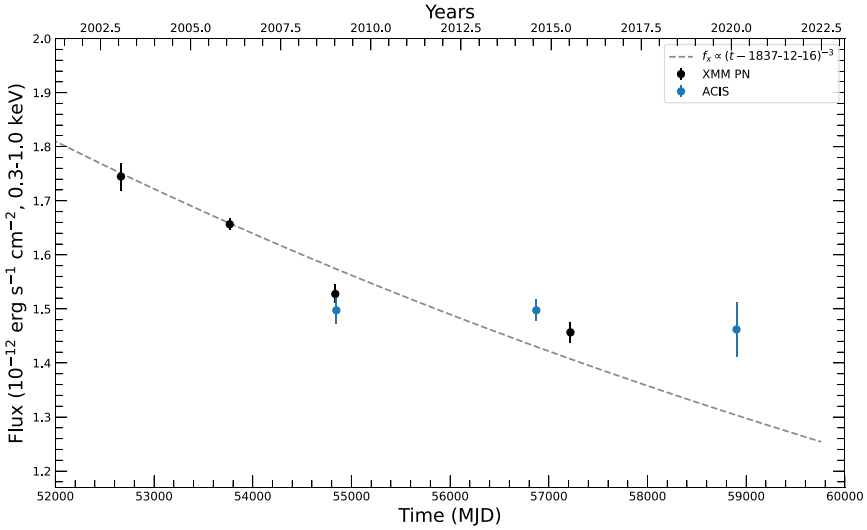

Figure 9. Comparison of soft-band fluxes (0.3–1.0 keV) from the XODF vs. time. The dashed line is a fit to the PN data assuming the X-ray flux declines as t^{-3}, as discussed in Espinoza-Galeas (2021).

pipeline processing and used the XMM-Newton SAS routine `evselect` to extract source and background spectra, and the routines `rmfgen` and `arfgen`, respectively, to calculate observation-specific responses and effective areas. For the ACIS observations, we extracted source spectra using an elliptical region centered on η Car with a semimajor axis of 36″ and semiminor axis of 26″. We used a circular region of 40″ radius to extract source spectra for the PN data. We extracted background spectra from source-free regions on the detector. For this analysis, we used version 4.14 of CIAO and version 4.9.7 of the CHANDRA CALDB, to minimize the effects of increased ACIS contamination on the low-energy response. We fit the ACIS and XMM-Newton-PN observations over the range 0.3–10 keV with a three-component `APEC` model with independent absorption (`TBabs`) for each component, and included an iron K fluorescence line at 6.4 keV, and calculated the flux in the soft XODF band (0.3–1.0 keV) for each spectrum.

The time dependence of the fluxes from 2003 to 2020 is shown in Figure 9. The PN fluxes show a significant, fairly linear decline from 2003 to 2015. The most recent ACIS flux measure, from March 2020, is about the same (or slightly higher) than the ACIS fluxes from the 2009 and 2014 observations. This is inconsistent with the linear decline as seen in the PN data, or the decline seen by NICER, as shown in Figure 9. A linear fit to the XMM-Newton-PN data would suggest that the XODF flux in 2020 should be about 16% less than the flux in 2009. This might indicate that the contamination correction for the ACIS low-energy effective area in 2020 was underestimated by ∼16%.

Assuming that the initial X-ray luminosity near the time of the Great Eruption was $L_x = 3 \times 10^{41}$ erg s^{-1}, and the velocity of this material was $V = 2000$ km s^{-1}, then the mass-loss rate of the high-velocity gas ejected during the Great Eruption was $\dot{M} = 2L_x/V^2 \sim 0.24\, M_\odot$ yr^{-1}. If the mass of the hot gas is $M = 0.012\, M_\odot$ as derived in Section 3, then the ejection of this fast material would have occurred on a timescale of only 18 days, assuming conservation of mass and that cooling of the hot material is negligible.

7. Conclusions

Our main conclusions are:

1. The combined soft-band X-ray image in the region around the massive binary η Car reveals a nearly uniform elliptical region of faint X-ray emission around the binary system extending beyond the bright X-ray emitting ring and beyond most of the bright optical nebulosities which make up the Outer Debris field, similar to the X-ray "bubble" noted by Mehner et al. (2016). We conclude that this faint elliptical shell is evidence of a blast wave from the 1843 eruption expanding into a wind-blown cavity in the circumstellar material around η Car, as previously suggested by Smith (2008). In this picture, the X-ray bright ring around η Car is produced when the blast wave collides with and shocks pre-existing clumps ejected in the 1200–1800 CE interval as discussed by Smith & Morse (2004) and Kiminki et al. (2016).
2. In addition, high spatial resolution X-ray images obtained by the CHANDRA/ACIS instrument over the past two decades demonstrate for the first time the expansion of features in the shocked X-ray emitting ring which surrounds η Car at a distance of about 0.5 arcmin. This expansion is clearly demonstrated by a comparison of the brightness profiles of the XODF in 1999 and 2020, which shows that the peak brightness of the XODF expanded by about 3″ from η Car in that interval.
3. We derive for the first time proper-motion of four bright X-ray emitting knots associated with previously identified optical structures known as the "S-condensation" and "S-ridge," a bright diffuse X-ray emitting structure near the "W-arc" and a region of shocked gas near the "E-condensations." The images are not deep enough to conclusively determine proper motions in fainter diffuse structures toward the south and east. While X-ray expansion has been measured for some X-ray bright knots in Galactic supernovae (for example, Sato & Hughes 2017; Sato et al. 2018; Millard et al. 2020) and the recurrent nova RS Oph (Montez et al. 2022), to our knowledge this is the first measurement of X-ray

expansion in ejecta from a star still in the nuclear burning stage.

4. If the ellipticity of the ring-like XODF is produced by a spatial gradient in ambient density, and if the blast wave is experiencing Sedov–Taylor expansion, then the morphology of the X-ray emitting ring indicates a variation of about a factor of 100 in particle density around the ring. It is probably more likely that the shape of the X-ray emission associated with the blast wave is due to some intrinsic initial condition of the eruption, given its similarity to the shape of the Homunculus nebula.
5. The ring-like structure of the X-ray emitting material in the XODF could naturally arise if the knots in the ODF were ejected in a preferred plane, as in the triple-star model of Smith et al. (2018a) and Hirai et al. (2021).
6. We show that a decline in soft-band flux from the XODF is seen in XMM-Newton PN spectra. This decline cannot be produced by variations of the central colliding wind binary source, since the contribution of colliding wind emission in this X-ray band is <1% because of the near total obscuration of any soft colliding wind X-rays by the large absorption column ($N_{\rm H} > 1 \times 10^{22}$ cm^2) of the Homunculus. This decline is similar to the soft-band decline first noted by Espinoza-Galeas (2021) from NICER monitoring observations. A simple model in which the emission measure declines with time as t^{-3} indicates that, very close to the Great Eruption, the X-ray luminosity of the blast wave was $\sim 10^{41}$ erg s^{-1}, which is approaching (if not exceeding) the total luminosity of the eruption at longer wavelengths. Smith (2013) already suggested that the radiant energy of the blast wave also had roughly equal kinetic energy to the Homunculus; our results suggest equipartition of energy between the X-ray luminosity of the fastest ejecta in the blast wave, the energy radiated at lower energies, and the kinetic power of Homunculus.
7. If the mass of the fast X-ray emitting material ejected during the Great Eruption is conserved, and cooling is negligible since the time of ejection, then the ejection occurred over a timescale $\tau \sim 18$ days. Thus the ejection of the fast, low-density material occurred on a very short timescale compared to the ∼year-long ejection (Smith 2017) of the slow, dense material which formed the Homunculus. This suggests that the Great Eruption first produced a rapid ejection of a small amount of fast, low-density material which produced the X-ray blast wave, followed by the slower ejection of dense material that eventually formed the Homunculus Nebula.

D. Espinoza-Galeas gratefully acknowledges support from NASA grants #80NSSC19K1451 and #80NSSC21K0092, and SAO grant #GO9-20015A thru NASA. The material is based upon work supported by NASA under award number 80GSFC21M0002. C. M. P. Russell was supported by SAO grant #GO0-21006A through NASA; this support is gratefully acknowledged. AFJM is grateful for financial support from NSERC (Canada). This research has made use of data obtained from the CHANDRA Data Archive and the CHANDRA Source Catalog, and the CIAO software package (Fruscione et al. 2006) provided by the CHANDRA X-ray Center, and Sherpa (Doe et al. 2007; Burke et al. 2020). This research has also made use of the XMM-Newton Science Analysis System Gabriel et al. (2004). This research has made use of data and software provided by the High Energy Astrophysics Science Archive Research Center (HEASARC), which is a service of the Astrophysics Science Division at NASA/GSFC. This research has made use of NASA's Astrophysics Data System, and Astropy,[16] a community-developed core Python package for Astronomy (Astropy Collaboration et al. 2013, 2018). This research made use of the DS9 image viewer (Joye & Mandel 2005) which is supported by funding from the CHANDRA X-ray Science Center (CXC), the HEASARC, and the JWST Mission office at the Space Telescope Science Institute. This paper was typeset using the PythonTex package (Poore 2015).

ORCID iDs

Michael F. Corcoran https://orcid.org/0000-0002-7762-3172
K. Hamaguchi https://orcid.org/0000-0001-7515-2779
Nathan Smith https://orcid.org/0000-0001-5510-2424
I. R. Stevens https://orcid.org/0000-0001-7673-4340
A. F. J. Moffat https://orcid.org/0000-0002-4333-9755
Noel D. Richardson https://orcid.org/0000-0002-2806-9339
Gerd Weigelt https://orcid.org/0000-0001-9754-2233
David Espinoza-Galeas https://orcid.org/0000-0003-2971-0439
Augusto Damineli https://orcid.org/0000-0002-7978-2994
Theodore R. Gull https://orcid.org/0000-0002-6851-5380

References

Astropy Collaboration, Price-Whelan, A. M., SipHocz, B. M., et al. 2018, AJ, 156, 123
Astropy Collaboration, Robitaille, T. P., Tollerud, E. J., et al. 2013, A&A, 558, A33
Borkowski, K. J., Lyerly, W. J., & Reynolds, S. P. 2001, ApJ, 548, 820
Burke, D., Laurino, O., Wmclaugh, et al. 2020, sherpa/sherpa: Sherpa v4.12.1, Zenodo, doi:10.5281/zenodo.3944985
Chlebowski, T., Seward, F. D., Swank, J., & Szymkowiak, A. 1984, ApJ, 281, 665
Corcoran, M. F., Rawley, G. L., Swank, J. H., & Petre, R. 1995a, ApJL, 445, L121
Corcoran, M. F., Swank, J., Rawley, G., et al. 1995b, RMxAC, 2, 97
Currie, D. G., Dowling, D. M., Shaya, E. J., et al. 1996, AJ, 112, 1115
Damineli, A., Navarete, F., Hillier, D. J., et al. 2021, MNRAS, 505, 963
Davidson, K., Dufour, R. J., Walborn, N. R., & Gull, T. R. 1986, ApJ, 305, 867
Davidson, K., & Humphreys, R. M. 1997, ARA&A, 35, 1
Davidson, K., Smith, N., Gull, T. R., Ishibashi, K., & Hillier, D. J. 2001, AJ, 121, 1569
Davidson, K., Walborn, N. R., & Gull, T. R. 1982, ApJL, 254, L47
Doe, S., Nguyen, D., Stawarz, C., et al. 2007, in ASP Conf. Ser. 376, Astronomical Data Analysis Software and Systems XVI, ed. R. A. Shaw, F. Hill, & D. J. Bell (San Francisco, CA: ASP), 543
Ebbets, D., Malumuth, E., Davidson, K., White, R., & Walborn, N. 1993, in ASP Conf. Ser. 35, Massive Stars: Their Lives in the Interstellar Medium, ed. J. P. Cassinelli & E. B. Churchwell (San Francisco, CA: ASP), 263
Espinoza-Galeas, D. A. 2021, PhD thesis, The Catholic University of America
Espinoza-Galeas, D., Corcoran, M. F., Hamaguchi, K., et al. 2022, ApJ, 933, 136
Evans, I. N., Primini, F. A., Miller, J. B., et al. 2020, AAS Meeting Abstracts, 235, 154.05
Fruscione, A., McDowell, J. C., Allen, G. E., et al. 2006, Proc. SPIE, 6270, 62701V
Gabriel, C., Denby, M., Fyfe, D. J., et al. 2004, in ASP Conf. Ser. 314, Astronomical Data Analysis Software and Systems (ADASS) XIII, ed. F. Ochsenbein, M. G. Allen, & D. Egret (San Francisco, CA: ASP), 759
Gaviola, E. 1950, ApJ, 111, 408

[16] http://www.astropy.org

Herschel, J. F. W., Sir 1838, MNRAS, 4, 121
Hillier, D. J., Davidson, K., Ishibashi, K., & Gull, T. 2001, ApJ, 553, 837
Hirai, R., Podsiadlowski, P., Owocki, S. P., Schneider, F. R. N., & Smith, N. 2021, MNRAS, 503, 4276
Joye, W. A., & Mandel, E. 2005, in ASP Conf. Ser. 347, Astronomical Data Analysis Software and Systems XIV, ed. P. Shopbell, M. Britton, & R. Ebert (San Francisco, CA: ASP), 110
Kiminki, M. M., Reiter, M., & Smith, N. 2016, MNRAS, 463, 845
Lamers, H. J. G. L. M., Livio, M., Panagia, N., & Walborn, N. R. 1998, ApJL, 505, L131
Leutenegger, M. A., Kahn, S. M., & Ramsay, G. 2003, ApJ, 585, 1015
Mehner, A., Steffen, W., Groh, J. H., et al. 2016, A&A, 595, A120
Millard, M. J., Bhalerao, J., Park, S., et al. 2020, ApJ, 893, 98
Montez, R., Luna, G. J. M., Mukai, K., Sokoloski, J. L., & Kastner, J. H. 2022, ApJ, 926, 100
Morris, P. W., Gull, T. R., Hillier, D. J., et al. 2017, ApJ, 842, 79
Morse, J. A., Kellogg, J. R., Bally, J., et al. 2001, ApJL, 548, L207
Pittard, J. M., & Corcoran, M. F. 2002, A&A, 383, 636
Poore, G. M. 2015, CS&D, 8, 014010
Rest, A., Prieto, J. L., Walborn, N. R., et al. 2012, Natur, 482, 375
Sato, T., & Hughes, J. P. 2017, ApJ, 845, 167
Sato, T., Katsuda, S., Morii, M., et al. 2018, ApJ, 853, 46
Seward, F. D., Butt, Y. M., Karovska, M., et al. 2001, ApJ, 553, 832
Seward, F. D., & Chlebowski, T. 1982, ApJ, 256, 530
Seward, F. D., Forman, W. R., Giacconi, R., et al. 1979, ApJL, 234, L55
Smith, N. 2006, ApJ, 644, 1151
Smith, N. 2008, Natur, 455, 201
Smith, N. 2013, MNRAS, 429, 2366
Smith, N. 2017, MNRAS, 471, 4465
Smith, N., Andrews, J. E., Rest, A., et al. 2018a, MNRAS, 480, 1466
Smith, N., & Frew, D. J. 2011, MNRAS, 415, 2009
Smith, N., & Gehrz, R. D. 1998, AJ, 116, 823
Smith, N., Gehrz, R. D., Hinz, P. M., et al. 2003, AJ, 125, 1458
Smith, N., & Morse, J. A. 2004, ApJ, 605, 854
Smith, N., Rest, A., Andrews, J. E., et al. 2018b, MNRAS, 480, 1457
Soker, N. 2004, ApJ, 612, 1060
Thackeray, A. D. 1949, Obs, 69, 31
Walborn, N. R. 1976, ApJL, 204, L17
Walborn, N. R., & Blanco, B. M. 1988, PASP, 100, 797
Walborn, N. R., Blanco, B. M., & Thackeray, A. D. 1978, ApJ, 219, 498
Weis, K., Corcoran, M. F., Bomans, D. J., & Davidson, K. 2004, A&A, 415, 595
Weis, K., Duschl, W. J., & Bomans, D. J. 2001, A&A, 367, 566
Woosley, S. E. 2017, ApJ, 836, 244